Chinese Chemical Letters 36 (2025) 110063

Contents lists available at ScienceDirect

Chinese Chemical Letters

journal homepage: www.elsevier.com/locate/cclet

Ultrafast spray pyrolysis for synthesizing uniform Mg-doped $LiNi_{0.9}Co_{0.05}Mn_{0.05}O_2$

Junhao Dai[a,b], Zhu He[a], Xinhai Li[a,c], Guochun Yan[a,c], Hui Duan[a,c], Guangchao Li[a,c], Zhixing Wang[a,c], Huajun Guo[a,c], Wenjie Peng[a,c], Jiexi Wang[a,c,*]

[a] National Energy Metal Resources and New Materials Key Laboratory, Engineering Research Center of the Ministry of Education for Advanced Battery Materials, Hunan Provincial Key Laboratory of Nonferrous Value-Added Metallurgy, School of Metallurgy and Environment, Central South University, Changsha 410083, China
[b] School of Materials Science and Engineering, Central South University, Changsha 410083, China
[c] National Engineering Research Centre of Advanced Energy Storage Materials, Changsha 410205, China

ARTICLE INFO

Article history:
Received 15 April 2024
Revised 13 May 2024
Accepted 27 May 2024
Available online 28 May 2024

Keywords:
Ultrafast synthesis
Lithium ion battery
Spray pyrolysis
$LiNi_{0.9}Co_{0.05}Mn_{0.05}O_2$
Homogeneous doping

ABSTRACT

Nickel-rich cathode materials have received widespread attention due to their high energy density. However, the poor rate capability and inferior cycle stability seriously hinder their large-scale application. The traditional co-precipitation method for preparing them has a long process and easily arises agglomeration leading to inhomogeneous element distribution. Here, a novel precursor containing Li element was prepared by ultrafast spray pyrolysis (SP) in 3–5 s. Then the precursor was used to synthesize pristine $LiNi_{0.9}Co_{0.05}Mn_{0.05}O_2$ (NCM90) and 1% Mg modified $LiNi_{0.9}Co_{0.05}Mn_{0.05}O_2$ (NCM90-Mg1). This method gets rid of mixing Li/Mg source and the precursor prepared by common co-precipitation, thus could achieve homogeneous lithiation and Mg^{2+} doping. The cell parameter *c* is expanded, and the cation disorder is reduced after Mg^{2+} doping. Furthermore, the harmful H2-H3 phase transition in NCM90-Mg1 is also well suppressed. As a result, the obtained NCM90-Mg1 shows better electrochemical performance than NCM90. Within 2.8–4.3 V (25 °C), the specific discharge capacity of NCM90-Mg1 at 5 C is as high as 169.1 mAh/g, and an outstanding capacity retention of 70.0% (10.0% higher than NCM90) can be obtained after 400 cycles at 0.5 C. At 45 °C, a capacity retention of 81.9% after 100 cycles at 1 C is recorded for NCM90-Mg1. Moreover, the NCM90-Mg1 also exhibits superior cycle stability when cycled at high cut-off voltage (4.5 V, 25 °C), possessing the capacity retention of 79.2% after 200 cycles at 1 C. Therefore, SP can be proposed as a powerful method for the preparation of multi-element materials for next-generation high energy density LIBs.

In the recent years, demand for high-performance rechargeable batteries had become so ubiquitous, especially in the electric vehicle (EV) sector. Due to high power, energy densities and long cycle life, lithium ion batteries (LIBs) dominate the market of power batteries for EV [1-3]. In general, high specific energy LIBs depend on cathode materials with high specific capacity. Nickel-rich layered oxides $LiNi_xCo_yMn_zO_2$ $(x+y+z=1)$ (NCM) stands out for their high reversible capacity and energy density when Ni content is higher than 80%. Despite some promising properties, the issues of structure and capacity degeneration become increasingly serious with the increase of Ni content in NCM cathode materials [4-7]. The relevant changes in Nickel-rich layered cathode materials can be explained by the following issues: (1) Cation disordering (Li^+/Ni^{2+} disordering) leads to a transformation in the surface structure from layered to disordered, eventually forming rock-salt phase [8,9]. (2) The anisotropic shrinkage of lattices generates internal strain in deep delithiation, resulting in the formation of micro-cracks inside particles [10,11]. (3) The residual lithium including Li_2CO_3 and LiOH distributed on the surface of NCM cathode materials will induce interface side reaction between NCM cathode materials and electrolyte [12,13].

In order to overcome these limitations of nickel-rich layered cathode materials, many effects have been made, such as surface coating [14], ion doping [15], concentration-gradient NMC cathode materials [16] and preparation of dispersed single crystal [17]. Among these strategies, ion doping is an effective way to suppress H2-H3 phase transformation and cation disordering. It is believed that Mg^{2+} tends to migrate to the lithium layer, owing to its similar ionic radii with Li^+ ($r_{Mg^{2+}} = 0.72$ Å, $r_{Li^+} = 0.76$ Å) [18]. The Mg^{2+}

* Corresponding author.
E-mail address: wangjiexikeen@csu.edu.cn (J. Wang).

https://doi.org/10.1016/j.cclet.2024.110063
1001-8417/

ions occupy the lithium layer and act as pillar ions, which could stabilize the layered structure and reduce the anisotropic lattice distortion upon cycling [19].

It is a challenge for ion doping to achieve homogeneous element distribution, which determines the effect of doping. Spray pyrolysis (SP) is a popular strategy to show outstanding advantages in element distribution compared with typical co-precipitation methods, which is prone to arise agglomeration leading to inhomogeneous element distribution [20]. Many cathode materials have been prepared by SP using nitrates or acetates containing lithium as raw materials, such as $LiNi_{0.8}Co_{0.15}Al_{0.05}O_2$ [21], $LiNi_{0.8}Co_{0.1}Mn_{0.1}O_2$ [22], $LiNi_{1/3}Co_{1/3}Mn_{1/3}O_2$ [23-25]. In addition, the electrochemical properties of layered cathode materials were improved through *in situ* doping or coating by SP, such as glass LBO modified $LiCoO_2$ [26], Zr^{4+} doped $LiCoO_2$ [27], and Mo^{6+} doped $LiNi_xMn_yCo_{1-x-y}Mn_zO_2$ [28].

The main purpose of this study is to achieve homogeneous element doping by SP, which could enhance the electrochemical performance of the NCM90 cathode material effectively. A precursor containing Li, Ni, Co and Mn elements was prepared by SP using acetate solution. Then Ni-rich cathode material $LiNi_{0.9}Co_{0.05}Mn_{0.05}O_2$ (NCM90) was fabricated through high-temperature sintering. 1% Mg doped $LiNi_{0.9}Co_{0.05}Mn_{0.05}O_2$ (NCM90-Mg1) was also prepared through the same synthetic route with adding magnesium acetate to the precursor solution. Combining energy dispersive spectroscopy (EDS) and X-ray diffraction (XRD) with scanning electron microscopy (SEM), the results indicated that Mg^{2+} are doped homogeneously. The electrochemical performance of these cathode materials was tested under different conditions. The results indicated that rate capability and cycle stability of the NCM90-Mg1 were superior to the pristine NCM90 significantly.

The schematic for the synthetic route of desired cathode materials is shown in Fig. S1 (Supporting information). The precursor of NCM90 (P-NCM90) was prepared by SP at 55 °C. $LiC_2H_3O_2$, $Ni(C_2H_3O_2)_2{\cdot}4H_2O$, $Co(C_2H_3O_2)_2{\cdot}4H_2O$ and $Mn(C_2H_3O_2)_2{\cdot}4H_2O$ were dissolved in deionized water at a molar ratio of 1.07:0.9:0.05:0.05 with a concentration of 0.6 mol/L. Excess lithium was used to compensate for the loss during SP and sintering. After solute was fully dissolved, the solution was poured in a jacketed glass container with a 1.7 MHz ultrasonic nebulizer. O_2 as carrier gas carried atomized droplets into a vertical tubular furnace (VTL1200–1200–1200, Nanjing Boyuntong Instrument) at a speed of 5 L/min. The temperature of three chambers of the tubular furnace is 550 °C. The precursor powder was collected in nickel foam at the top of the tubular furnace. Then it was sintered at 720 °C in a tubular furnace (SK-B06123KF, Tianjing ZHONGHUAN) for 16 h in O_2 atmosphere to synthesize NCM90 cathode. The precursor of NCM90-Mg1 (P-NCM90-Mg1) and NCM90-Mg1 cathode were synthesized as the same route by adding $Mg(C_2H_3O_2)_2{\cdot}4H_2O$ to precursor solution. The molar ratio of Li:Ni:Co:Mn:Mg was 1.07:0.9:0.05:0.05:0.01.

Fig. 1a shows the XRD patterns of the precursors prepared by SP. The P-NCM90 and P-NCM90-Mg1 are mainly composed of NiO (PDF #44–1159) and Li_2CO_3 (PDF #22–1141), which are produced by the decomposition of $Ni(C_2H_3O_2)_2{\cdot}4H_2O$ and $LiC_2H_3O_2$, respectively. The characteristic peaks related to Mn, Co, and Mg are not detected, which may be due to their low content or doping in NiO. The XRD results indicate that the acetate decomposed completely. The SEM images of P-NCM90 and P-NCM90-Mg1 are shown in Figs. 1b and c, respectively. The particle size of precursor varies from several hundred nanometers to two microns. Due to the low solubility and poor permeability of acetate solution, the solute rapidly precipitates on the surface of the droplet and decomposes, accompanied by the inflation and break of the droplet to form contracted wrinkle morphology [21,29-31]. The morphology of precursors is largely determined by raw material, and there is no obvious difference in the morphology of two precursors because the raw materials are all acetate. To obtain well-layered cathode materials, the two precursors were both calcined at 720 °C for 16 h. The SEM images of the NCM90 and NCM90-Mg1 are shown in Figs. 1d and e. The secondary particles of these two materials both maintains the irregular sphericity of precursors, while the primary particles gradually grow to several hundred nanometers obviously. The primary particle surface of both samples is smooth particularly without residual impurities. There is no obvious difference by comparing the SEM images of these two materials, proving that the addition of Mg does not affect the morphology. The morphology changes from initial droplet to final product during the entire preparation process were displayed in Fig. 1f.

In order to investigate the influence of Mg doping on the Ni-rich materials, TEM analysis and EDS analysis were conducted. It can be seen from Figs. 2a and c that the secondary particles of the both samples after sintering are composed of several irregular nanoparticles, which are consistent with the above SEM images. By comparing Figs. 2b and d, both materials show clear lattice fringe. The lattice stripe spacing of the NCM90 and NCM90-Mg1 is calculated as 0.471 and 0.473 nm *via* Fourier transform respectively, implying that Mg doping enlarges the lithium-ion diffusion channels effectively [32]. In addition, the EDS elemental distribution mappings of NCM90-Mg1 are shown in Figs. 2f-i. It is clear that Ni, Co, Mn, and Mg are overlapped and distributed evenly, further proving that Mg^{2+} are distributed homogeneously by SP. To understand more crystal structural information, the Rietveld refinement results of XRD patterns of the pristine NCM90 and Mg-modified NCM90-Mg1 *via* Fullprof software are shown in Figs. 2j and k. All peaks can be well assigned to α-$NaFeO_2$-type structure (R-3m space group) without any impurity phase, indicating that Mg have been successfully embedded in layered structure of NCM90. The (006)/(102) and (108)/(110) peaks of these two materials apparently split, implying a well-ordered layered structure [33]. More detailed differences from Rietveld refinement results are shown in Table S1 (Supporting information). The small values of R_p and R_{wp} indicate the reliability of the results. The cell parameter *a* of the NCM90-Mg1 slightly increases compared with the NCM90. While the cell parameter *c* increases significantly, which is attributed to that Mg^{2+} with larger radius of 0.72 Å compared to these of the transition metal ions (Ni^{2+}: 0.69 Å, Ni^{3+}: 0.56 Å, Co^{3+}: 0.545 Å, Mn^{4+}: 0.53 Å) is more inclined to occupy the lithium layer during sintering [34,35]. Such increased *a* and *c* values is consistent with the above TEM images, further proofing that Mg doping could expend the Li^+ transmission channels in the NCM90-Mg1, which facilitates the diffusion of lithium ions, thus obtaining better rate performance [36]. It is easy to find that Mg enlarges the unit cell volume and *c*/*a* ratio. The NCM90-Mg1 has a smaller percentage of Ni^{2+} in 3b site of 2.176%, while that of the NCM90 is 3.038%. This means that the addition of Mg suppresses cation disordering (Li^+/Ni^{2+} disordering), which will cause the formation of rock-salt phases on surface during charging-discharging. Therefore, Mg doping enhances the crystal structure of Ni-rich materials, which will be beneficial to improving the electrochemical stability.

The electrochemical behaviors of the pristine and Mg doped samples are shown in Fig. 3. As shown in Fig. 3a, both samples deliver the similar initial discharge capacity (211.4 mAh/g *vs*. 210.9 mAh/g) and initial coulombic efficiency (85.2% *vs.* 85.6%) at 0.1 C. The rate and cycle performances of the two samples were tested between 2.8–4.3 V (25 °C). As shown in Fig. 3b, the average specific discharge capacity of NCM90 is 208.6, 203.8, 197.9, 190.0, 180.3 and 163.4 mAh/g at 0.1, 0.2, 0.5, 1, 2 and 5 C, respectively. In contrast, the average specific discharge capacity of NCM90-Mg1 is 207.7, 204.8, 199.4, 191.5, 182.8, and 169.1 mAh/g under the same current density, higher than those of NCM90 especially at 5 C. Moreover,

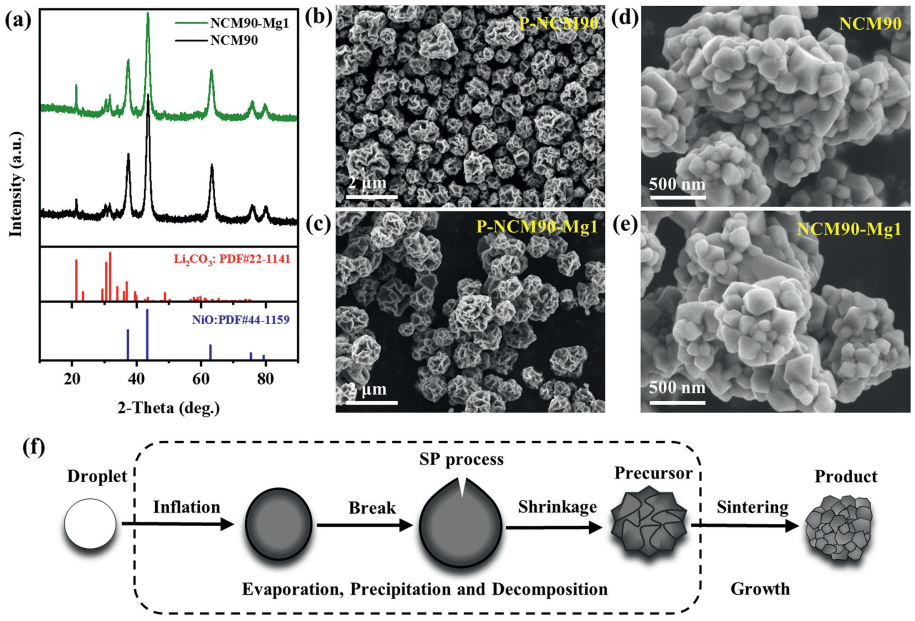

Fig. 1. Crystal structures and morphologies of as-prepared precursors. (a) XRD patterns; SEM images of (b) P-NCM90 and (c) P-NCM90-Mg1. SEM images of (d) NCM90 and (e) NCM90-Mg1. (f) Schematic diagram for morphological changes of the material during the entire preparation process.

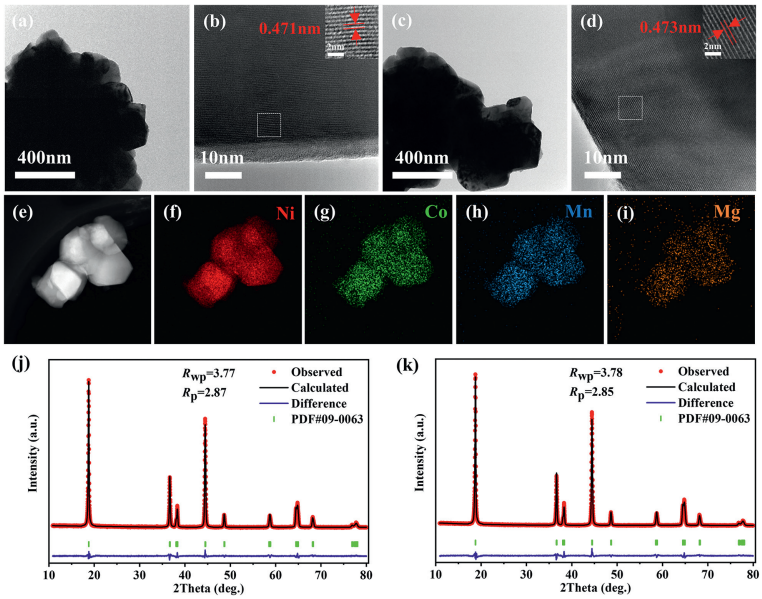

Fig. 2. Morphologies and crystal structures of as-prepared final materials. TEM images of (a, b) NCM90 and (c, d) NCM90-Mg1. (e-i) EDS elemental distribution mappings of Ni, Co, Mn, Mg. Rietveld refinement for XRD patterns of (j) NCM90 and (k) NCM90-Mg1.

NCM90-Mg1 can deliver an impressive average discharge capacity of 204.3 mAh/g when the current density resets to 0.1 C, very close to original average specific discharge capacity 207.7 mAh/g at 0.1 C. As presented in Fig. 3c, the NCM90 and NCM90-Mg1 deliver a similar initial discharge capacity of 199.5 and 198.2 mAh/g at 0.5 C. The tiny difference in discharge capacity can be explained by the reduction of Li^+ due to the addition of electrochemically inactive Mg^{2+} in the lithium layer. After 400 cycles, a higher capacity retention of 70.0% for the NCM90-Mg1 is observed, while that of the NCM90 is just 61.3%. Compared with the pristine NCM90, the cycle performance of NCM90-Mg1 was distinctly improved. Therefore, the Mg-doped NCM90-Mg1 demonstrates excellent rate performance and capacity retention, clearly indicating Mg doping enlarges the lithium-ion diffusion channels and enhances the stability of crystal structure [32]. For the sake of further demonstrating the electrochemical superiority of the Mg-modified Ni-rich cathode material NCM90-Mg1, cycling tests at higher cut-off potential (4.5 V) and higher temperature (45 °C) were conducted. Fig. 3d shows the comparison diagram of two samples between 2.8 V and 4.5 V at 25 °C. NCM90 and NCM90-Mg1 samples have a similar initial specific discharge capacity of 201.4 and 200.2 mAh/g at 1 C, respectively. After 200 cycles, the NCM90-Mg1 retains a higher reversible capacity of 158.5 mAh/g, corresponding to a capacity retention of 79.2%. By contrast, the NCM90 just displays a reversible capacity of 141.8 mAh/g with a lower capacity retention of 70.4%. The enhancement of electrochemical stability can also be observed within 2.8–4.3 V at 45 °C according to Fig. 3e. The NCM90-Mg1 fades from 201.4 mAh/g to 164.9 mAh/g with a capacity retention of 81.9% after 100 cycles at 1 C. While the NCM90 suffered a serious capacity loss from 202.6 mAh/g to 140.2 mAh/g with capacity

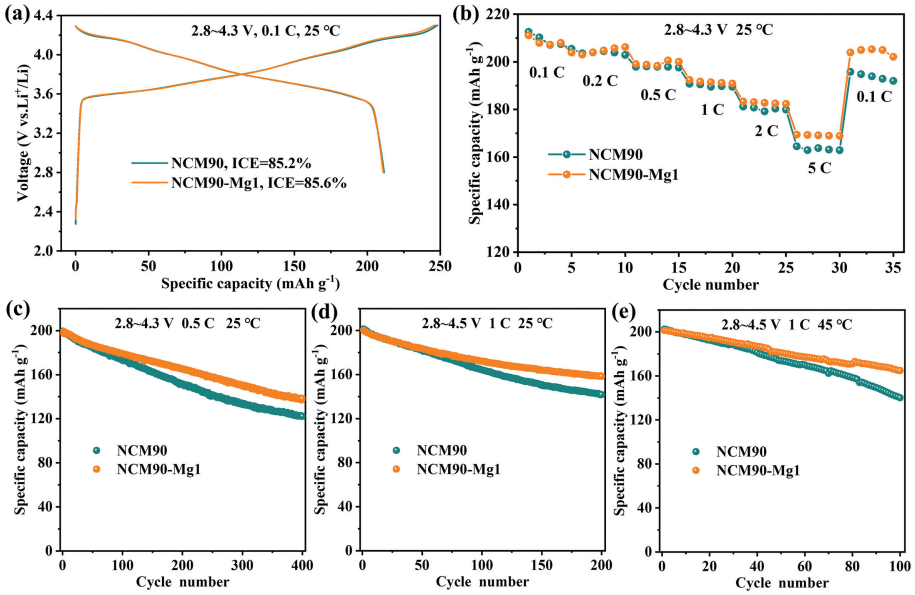

Fig. 3. Electrochemical performance of NCM90 and NCM90-Mg1. (a) Initial charge-discharge profile at 0.1 C. (b) Rate capability from 0.1 C to 5 C. Cycle performance under (c) 0.5 C, 25 °C and 2.8–4.3 V, (d) 1 C, 25 °C and 2.8–4.5 V; (e) 1 C, 25 °C and 45 °C.

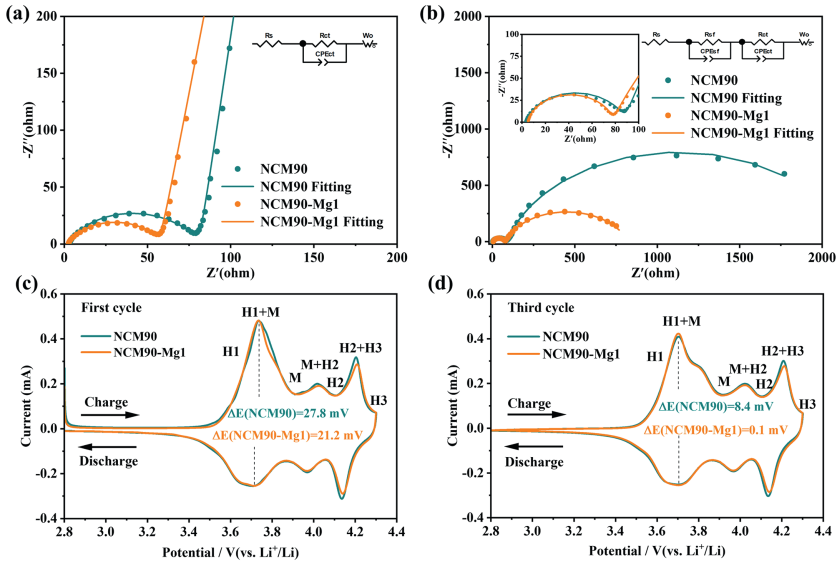

Fig. 4. Electrochemical Kinetics of NCM90 and NCM90-Mg1. Nyquist plots (a) before cycle and (b) after 200 cycles at 4.5 V and 1 C. (c, d) CV curves of (c) 1st cycle and (d) 3rd cycle in a scan rate of 0.1 mV/s at 25 °C within 2.8–4.3 V.

retention of only 69.2%. The above results indicate that Mg-doped NCM90-Mg1 has superior electrochemical stability whether at high voltage or high temperature.

Additionally, to study the effect of Mg^{2+} on electrode kinetics properties of NCM90, EIS and CV techniques were performed. Figs. 4a and b display the Nyquist diagram of the prepared two electrodes before cycle and after 200 cycles at 4.5 V. Fig. 4a contains one semicircle in the mid-high frequency ranges and a sloped straight line in low-frequency ranges, referring to charge-transfer resistance (R_{ct}) and Warburg impedance (W_o) respectively [37,38]. The first and second semicircles in Fig. 4b represent R_{sf} assigned to the film resistance and R_{ct} respectively after 200 cycles [39]. The corresponding fitting values are shown in Table S2 (Supporting information). The R_{ct} values of the NCM90 and NCM90-Mg1 before cycle are 71.7 Ω and 55.5 Ω respectively, indicating that the surface reconstruction layer on the NCM90-Mg1 cathode material surface is thinner. After 200 cycles, both R_{ct} and R_{sf} of the NCM90-Mg1 electrode both are significantly smaller than those of NCM90 electrode, meaning that the NCM90 cathode material surface has suffered more serious degradation and constructed thicker insulating solid electrolyte interphase at a higher cut-off voltage. The impedance test results are consistent with electrochemical behaviors and further prove that Mg^{2+} doping could reduce the surface reconstruction caused by cation mixing and stabilize bulk structure during charge-discharge process. As shown in Figs. 4c and d, CV curves of the first and third cycles of the two electrodes both exhibit three redox peaks corresponding to the phase transitions of hexagonal phase (H1) to monoclinic phase (M), monoclinic phase to hexagonal phase (H2) and hexagonal phase to hexagonal phase (H3) respectively during the extraction and insertion of Li^+ [40]. This means that Mg doping does not change the structure of the NCM90 material. The smaller the potential difference of redox peaks (ΔE), the better the reversibility electrode [41]. The CV results make known that the NCM90-Mg1 electrode has smaller ΔE

of 21.2 and 0.1 mV in the first and third cycles than those of the NCM90 electrode (27.8 and 8.4 mV). Anisotropic lattice expansion and contraction during H2-H3 phase transition lead to crack generation in bulk [42]. For the NCM90-Mg1 electrode, the peak intensity related to phase transition of H2-H3 is weaker than that of the NCM90 electrode, bearing out that the incorporation of Mg^{2+} into the lithium layer does restrain the phase transition of H2-H3. This is attributed to the fact that the material structure is stabilized by a "pillar" effect of Mg^{2+} in the lithium layer and the stronger Mg-O bond (−601 kJ/mol) than Ni-O bond (−489.5 kJ/mol) [19,42]. Consequently, the electrochemical performance of NCM90 has been improved prominently, especially at a higher cut-off voltage of 4.5 V and a higher temperature of 45 °C.

To sum up, in this work, pristine Ni-rich cathode material NCM90 and Mg-modified NCM90-Mg1 was synthesized through high-temperature sintering using a novel precursor prepared by fast SP, which is a convenient strategy to achieve homogeneous Mg^{2+} doping. The cation disorder was reduced and (003) plane spacing was expanded after the homogeneous addition of Mg. In addition, Mg^{2+} in the lithium layer could act as a "pillar" and the strong Mg-O bond also can stabilize the structure during cycling, so the harmful H2-H3 phase transition was suppressed. The NCM90-Mg1 represented excellent rate capability and cycle stability compared with the NCM90. Especially at 4.5 V high cut-off voltage (4.5 V) and high temperature (45 °C), the high capacity retention of 79.2% after 200 cycles and 81.9% after 100 cycles at 1 C was obtained respectively. In short, the superiority of Mg doping in the lithium layer to stabilize the structure of Ni-rich cathode materials has been demonstrated, and the SP method is also applicable to achieve homogeneous doping of arbitrary elements. Besides, SP method has huge potential for the scale applications in battery industry as a convenient and ultrafast method to prepare homogeneous elements doped precursors. Therefore, a fresh strategy for preparing the next generation of high energy density LIBs is provided.

Declaration of competing interest

The authors declare that they have no known competing financial interests or personal relationships that could have appeared to influence the work reported in this paper.

CRediT authorship contribution statement

Junhao Dai: Writing – original draft, Methodology, Investigation, Formal analysis, Conceptualization. **Zhu He:** Writing – original draft, Methodology, Investigation, Formal analysis, Data curation, Conceptualization. **Xinhai Li:** Visualization, Resources, Project administration, Formal analysis. **Guochun Yan:** Formal analysis. **Hui Duan:** Formal analysis. **Guangchao Li:** Formal analysis. **Zhixing Wang:** Formal analysis. **Huajun Guo:** Formal analysis. **Wenjie Peng:** Formal analysis. **Jiexi Wang:** Writing – review & editing, Visualization, Supervision.

Acknowledgments

This work was supported by the National Natural Science Foundation of China (No. 52122407) and the Science and Technology Innovation Program of Hunan Province (No. 2022RC3048). We also thank BASF Shanshan Battery Material Co., Ltd. for financial support.

Supplementary materials

Supplementary material associated with this article can be found, in the online version, at doi:10.1016/j.cclet.2024.110063.

References

[1] M. Li, J. Lu, Z. Chen, et al., Adv. Mater. 30 (2018) 1800561.
[2] Z. Jiang, S. Chen, C. Wei, et al., Chin. Chem. Lett. 35 (2024) 108561.
[3] S. Yang, B. Wang, Q. Lv, et al., Chin. Chem. Lett. 34 (2023) 107783.
[4] A. Aishova, G.T. Park, C.S. Yoon, et al., Adv. Energy Mater. 10 (2019) 1903179.
[5] W. Liu, P. Oh, X. Liu, et al., Angew. Chem. Int. Ed. 54 (2015) 4440–4457.
[6] H.H. Ryu, K.J. Park, C.S. Yoon, et al., Chem. Mater. 30 (2018) 1155–1163.
[7] R. Yue, F. Xia, R. Qi, et al., Chin. Chem. Lett. 32 (2021) 849–853.
[8] J. Zheng, Y. Ye, T. Liu, et al., Acc. Chem. Res. 52 (2019) 2201–2209.
[9] X. Wang, B. Zhang, Z. Xiao, et al., Chin. Chem. Lett. 34 (2023) 107772.
[10] C. Wang, L. Shao, X. Guo, et al., ACS Appl. Mater. Interfaces 11 (2019) 44036–44045.
[11] Z. Wang, H. Zhu, H. Yu, et al., Chin. Chem. Lett. 34 (2023) 107718.
[12] A.O. Kondrakov, H. Geßwein, K. Galdina, et al., J. Phys. Chem. C 121 (2017) 24381–24388.
[13] L. Mu, R. Lin, R. Xu, et al., Nano Lett. 18 (2018) 3241–3249.
[14] P. Yan, J. Zheng, J. Liu, et al., Nat. Energy 3 (2018) 600–605.
[15] C. Lv, J. Yang, Y. Peng, et al., Electrochim. Acta 297 (2019) 258–266.
[16] J. Kim, H. Cho, H.Y. Jeong, et al., Adv. Energy Mater. 7 (2017) 1602559.
[17] X. Fan, G. Hu, B. Zhang, et al., Nano Energy 70 (2020) 104450.
[18] Y.Y. Wang, X. Song, S. Liu, et al., ACS Appl. Mater. Interfaces 13 (2021) 56233–56241.
[19] Q. Xie, W. Li, A. Manthiram, Chem. Mater. 31 (2019) 938–946.
[20] B. You, Z. Wang, F. Shen, et al., Small Methods 5 (2021) 2100234.
[21] J.N. Zhang, S.Q. Xu, K.I. Hamad, et al., Powder Technol. 363 (2020) 1–6.
[22] B.Z. You, J.P. Sun, Y. Jing, et al., ACS Appl. Mater. Interfaces 15 (2023) 14587–14595.
[23] J. Li, S. Xiong, Y. Liu, et al., Nano Energy 2 (2013) 1249–1260.
[24] M. Oljaca, B. Blizanac, A.Du Pasquier, et al., J. Power Sources 248 (2014) 729–738.
[25] Y. Wang, J. Roller, R. Maric, ACS Omega 3 (2018) 3966–3973.
[26] S.H. Choi, J.H. Kim, Y.N. Ko, et al., J. Power Sources 244 (2013) 129–135.
[27] S.H. Kim, C.S. Kim, J. Electroceram. 23 (2008) 254–257.
[28] B. Pişkin, C. Savaş Uygur, M.K. Aydınol, Int. J. Energ. Res. 42 (2018) 3888–3898.
[29] Y. Li, X. Li, Z. Wang, et al., J. Alloys Compd. 696 (2017) 836–843.
[30] J. Leng, Z. Wang, J. Wang, et al., Chem. Soc. Rev. 48 (2019) 3015–3072.
[31] J. Zhang, G. Singh, S. Xu, et al., J. Clean. Prod. 271 (2020) 122518.
[32] B. Zhang, L. Cheng, P. Deng, et al., J. Alloys Compd. 872 (2021) 159619.
[33] A.K. Arof, J. Alloys Compd. 449 (2008) 288–291.
[34] F. Peng, Y.Q. Chu, Y. Li, et al., J. Energy Chem. 71 (2022) 434–444.
[35] A. Liu, N. Zhang, H. Li, et al., J. Electrochem. Soc. 166 (2019) A4025–A4033.
[36] L. Li, Z. Zhang, S. Fu, et al., Appl. Surf. Sci. 476 (2019) 1061–1071.
[37] M.H. Chu, Z.Y. Huang, T.E. Zhang, et al., ACS Appl. Mater. Interfaces 13 (2021) 19950–19958.
[38] L. Cheng, Y.A. Zhou, B. Zhang, et al., Chem. Eng. J. 452 (2023) 139336.
[39] H. Kim, D. Byun, W. Chang, et al., J. Mater. Chem. A 5 (2017) 25077–25089.
[40] Q.Q. Tao, L.G. Wang, C.H. Shi, et al., Mater. Chem. Front. 5 (2021) 2607–2622.
[41] S. Jamil, G. Wang, L. Yang, et al., J. Mater. Chem. A 8 (2020) 21306–21316.
[42] T. Yoshida, K. Hongo, R. Maezono, J. Phys. Chem. C 123 (2019) 14126–14131.